Wireless 3D Surgical Navigation and Tracking System with 100μm Accuracy Using Magnetic-Field Gradient-Based Localization

Saransh Sharma, Aditya Telikicherla, Grace Ding, Fatemeh Aghlmand, Arian Hashemi Talkhooncheh, Mikhail G. Shapiro, Azita Emami

***Abstract*—This paper describes a high-resolution 3D navigation and tracking system using magnetic field gradients, that can replace X-Ray fluoroscopy in high-precision surgeries. Monotonically varying magnetic fields in X, Y and Z directions are created in the field-of-view (FOV) to produce magnetic field gradients, which encode each spatial point uniquely. Highly miniaturized, wireless and battery-less devices, capable of measuring their local magnetic field, are designed to sense the gradient field. One such device can be attached to an implant inside the body and another to a surgical tool, such that both can simultaneously measure and communicate the magnetic field at their respective locations to an external receiver. The relative location of the two devices on a real-time display can enable precise surgical navigation without using X-Rays. A prototype device is designed consisting of a micro-chip fabricated in 65nm CMOS technology, a 3D magnetic sensor and an inductor-coil. Planar electro-magnetic coils are designed for creating the 3D magnetic field gradients in a 20x20x10cm^3 of scalable FOV. Un-ambiguous and orientation-independent spatial encoding is achieved by: (i) using the gradient in the total field magnitude instead of only the Z-component; and (ii) using a combination of the gradient fields to correct for the non-linearity and non-monotonicity in X and Y gradients. The resultant X and Y FOV yield ≥90% utilization of their respective coil-span. The system is tested *in vitro* to demonstrate a localization accuracy of <100μm in 3D, the highest reported to the best of our knowledge.**

***Index Terms*—ASIC, CMOS, electromagnet, gradient coil, implantable, localization, magnetic field, magnetic field gradient, magnetic sensor, micro-chip, MRI, navigation, orthopedic surgery, position encoding, precision surgery, tracking, wireless, X-Ray fluoroscopy, 13.56MHz, 3D.**

I. Introduction

LOCALIZATION and real-time tracking of devices *in vivo* with high precision are required during many surgical procedures and medical diagnostic techniques. For instance, in orthopedic surgeries, long bone fractures are fixed by putting a metal rod into the bone and holding the two together using screws. It is crucial to know the precise location of the screw-holes before drilling into the fractured bone to put the screws in place [1]. Currently, multiple X-Ray images are taken to locate the screw-holes. In addition to orthopedic surgeries, precise localization inside the body has many other medical applications. In capsule endoscopy, a pill-shaped camera is sent through the gastrointestinal (GI) tract of a patient, taking images of different regions of the stomach and intestines. It is important to know the real-time location of the pill as it goes through the GI tract, to provide spatiotemporal mapping for better diagnosis [2]. Currently, X-Ray imaging is used to find the pill's location at a given time. Another notable example is robotic surgery, which requires highly precise movement of surgical tools inside the body. Other applications where localization and tracking are critical include laparoscopic surgery and cardiovascular procedures [3]. All of these scenarios illustrate the importance of precise real-time navigation and localization of devices *in vivo*, which currently relies heavily on potentially harmful X-Ray radiation. Typical imaging resolution of 200-500μm can be obtained by clinically used X-Ray imagers and computed tomography (CT) systems, which can be improved to <50μm using high radiation doses [4]. Multiple 2D X-Ray images can be used to provide detailed, 360^0 cross-sectional images, using CT [3].

In this work, we focus on orthopedic surgery, a major class of medical procedures performed on millions of patients per year [5]. Orthopedic surgeries are performed for the repair, reconstruction, and replacement of various bones and joints. Intramedullary (IM) nailing is a common example of high-precision orthopedic surgery, which requires insertion of a Titanium (Ti) metal rod into the medullary canal of a fractured bone, followed by locking screws [1]. The screws are installed at the proximal and distal end of the bone with the help of a surgical drill, to hold the bone and rod together. X-Ray fluoroscopy is performed over the desired region to precisely locate the screw-holes and their axis, before drilling manually. This is called the free-hand technique. Fluoroscopy is used because it can produce real-time images on a screen by using continuous X-Ray beams, which provide real-time feedback to the surgeon during the procedure [6]. The total duration of fluoroscopy can vary from 1-15 min per patient and is highly

Manuscript received September 1, 2020; revised January 27, 2021 and March 10, 2021; accepted March 30, 2021. This work was supported in part by the National Science Foundation under Grant No. 1823036, in part by the Rothenberg Innovation Initiative under Grant No. 101170 and in part by the Heritage Medical Research Institute.

S. Sharma, A. Telikicherla, G. Ding, F. Aghlmand, A.H. Talkhooncheh, and A. Emami are with the department of Electrical Engineering, California Institute of Technology (Caltech), Pasadena, CA 91125 USA (e-mail: ssharma3@caltech.edu).

M.G. Shapiro is with the department of Chemical Engineering, California Institute of Technology (Caltech), Pasadena, CA 91125 USA.

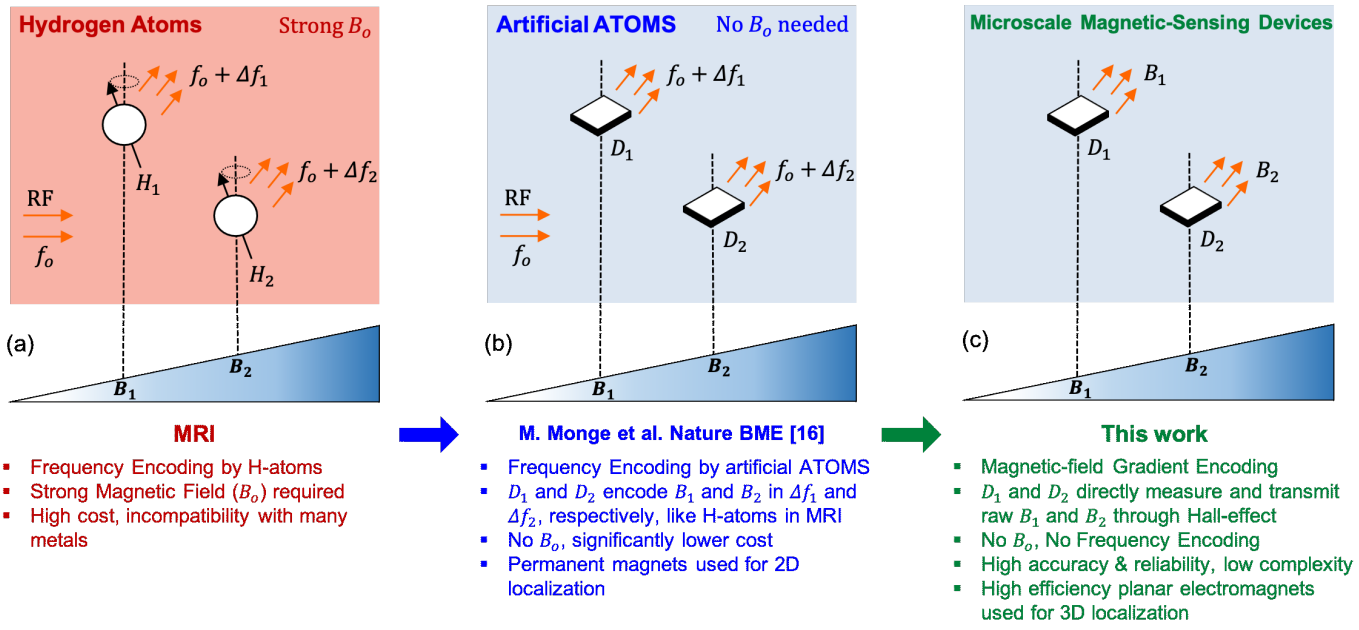

Fig. 1. (a) Frequency encoding performed in MRI using hydrogen atoms. (b) Micro-chips working as artificial atoms to perform frequency encoding without any B_0 [16]. (c) Micro-chips localized using magnetic-field gradient encoding, eliminating both B_0 and frequency encoding in this work.

dependent on the skills of the surgeon [7]. This can cause high levels of radiation exposure to the patient, surgeon and staff. Despite the drawback, the freehand technique using X-Ray fluoroscopy remains the gold standard for localizing screw-holes in bone implants, achieving 100-200μm of accuracy, depending on the radiation dose [3]-[4]. Other medical procedures requiring precise alignment and positioning of surgical tools and implants, almost exclusively use X-Ray fluoroscopy instead of 2D X-Ray images, the latter being more common for diagnosis and snapshots [3].

While there are several alternative non-ionizing methods for imaging and localization, none of them provide enough resolution and/or field-of-view (FOV) [8]. Most existing radio-frequency (RF) methods in the sub-GHz to several GHz of frequency range (as a trade-off between tissue-absorption loss and antenna-size of the implant), are based on the received signal strength, time of flight, time difference of arrival, angle of arrival and usage of RFID tags. However, such RF signals suffer very high attenuation when propagating through the human tissue. Severe multipath effects further limit their use for *in vivo* localization [9]. Ultrasound-based methods are most effective for soft tissues like muscles, tendons and internal organs, but have poor performance for bones and gas cavities, and require contact coupling to the subject [10]-[11]. Optical methods based on tracking infrared light, laser beam and fluorescence microscopy are limited by their low imaging depth due to light attenuation caused by absorption and scattering [11]-[13]. Handheld mechanical tools are also available for screw-hole localization. However, they work well for proximal holes but not for distal holes because of the high axial deformation (≈15mm) of the metal rod as it goes inside the bone [7], which cannot be compensated by the mechanical guide.

In this paper, we present a radiation-free system for high-precision surgical alignment, navigation and tracking, using magnetic-field gradient-based localization of micro-scale devices. The system concept and overview are described in Section-II. Design of the micro-scale devices is covered in Section-III. Section-IV consists of a detailed explanation of the magnetic field gradient (generation and characterization) and the localization technique. Measurement results of the entire system under different scenarios are described in Section-V and finally, Section-VI concludes the paper.

II. System Concept and Overview

In contrast to X-Rays, RF, ultrasound and visible light, static magnetic fields (up to 5-10T) have negligible attenuation through the human body, no dependency on the tissue type, and no known harmful effects on cells [14]-[15]. These properties make magnetic resonance imaging (MRI) a very powerful and widely useful imaging tool. In a typical MRI sequence, a strong and static magnetic field B_0, commonly ranging from 1.5-7T, is applied to polarize the nuclear spins of hydrogen atoms. Thereafter, a known RF frequency of f_0 (Larmor frequency) is applied to excite the nuclei to precess at f_0. In the read-out phase, the RF is turned off and a magnetic field gradient is applied over the region to be imaged. During this phase, the nuclei radiate at f_0, shifted by a small amount that is a function of the applied magnetic field gradient. This approach is called frequency encoding, wherein the frequency shifts of Δf_1 and delta Δf_2 contain the spatial information of atomic nuclei, as shown in Fig. 1 (a). As a result, MRI can achieve 100μm-1mm imaging resolution, which is comparable to the accuracy obtained from X-Ray imaging. However, the high cost of MRI equipment (mainly because of the very strong B_0) and its incompatibility with many metals, make it an impractical modality to be used in real time during orthopedic procedures.

As shown in [16], micro-chip devices can be designed to mimic the behavior of nuclear spins inside the body, and frequency encoding can be performed with these artificial

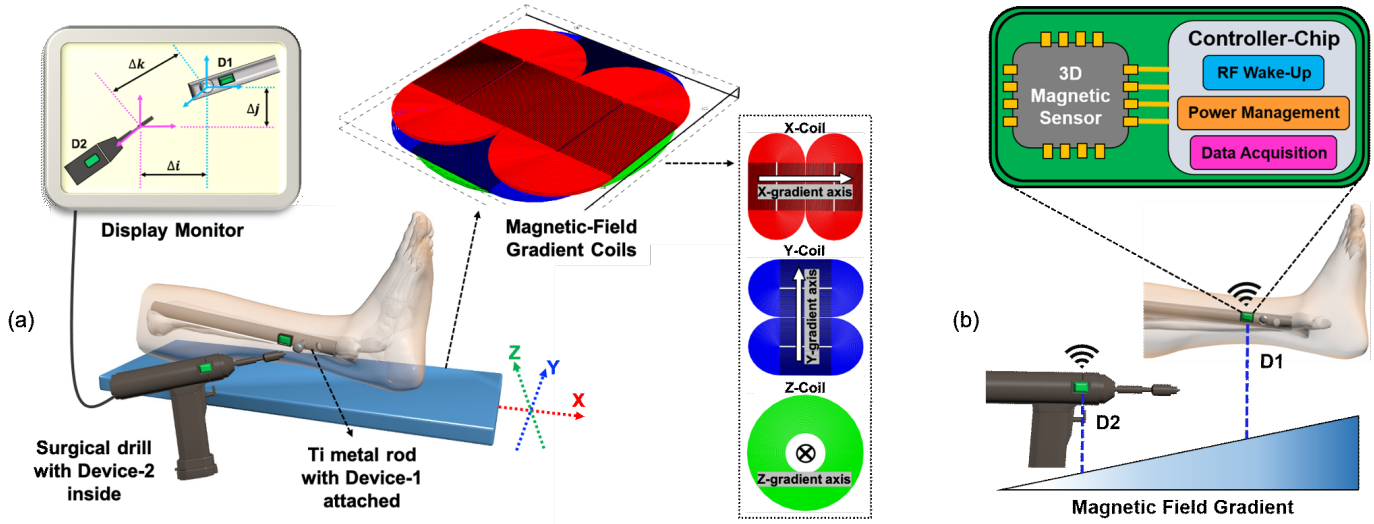

Fig. 2. (a) Complete overview of the localization technique. Devices 1 and 2 measure the magnetic field at their respective locations, generated by the gradient coils, and their relative position is displayed in real time. (b) Principle of opeartion of the gradient-based localization of devices.

atoms, similar to MRI. A simplified view of the system in [16] is shown in Fig. 1 (b), wherein devices D_1 and D_2 are excited using an RF frequency of f_0, and transmit a frequency-encoded signal during their read-out phase. The absence of strong background B_0 in [16] is a major difference from MRI, which reduces the cost of implementation significantly. Such a system is particularly useful when communicating with a large number of devices simultaneously over different frequency bands.

In this work, we describe an approach focused on achieving higher precision while communicating with a small number of wireless devices, as required in surgical applications. Rather than relying on analog frequency encoding, this approach uses digital reporting of the total magnetic field value at the devices' location, in combination with 3D field gradients, to precisely and robustly track the location of wireless devices. Micro-chip devices D_1 and D_2 are designed to *directly* measure, digitize, and transmit their local magnetic fields B_1 and B_2, respectively, through the Hall-effect, as shown is shown in Fig. 1 (c). Direct measurement of the raw field value at the devices' location eliminates the conversion complexity (required in frequency encoding), improves the accuracy, and enhances the reliability of the system. Other advantages of our system compared to [16] and other EM-based tracking techniques are the completely wireless operation of the devices D_1 and D_2, scalable and high FOV using efficient planar-electromagnets, and 3D localization with 100µm accuracy, as detailed below.

The complete system overview and the principle of operation of the proposed localization technique are shown in Fig. 2. In a surgical procedure, the patient's leg with a Ti metal rod inside is placed on top of a bed. Our system is designed such that a small electronic device (shown in green) can be attached right next to the screw-hole at a known position on the rod. Another identical device can be installed on the surgical drill. A planar electromagnetic assembly, consisting of magnetic field gradient generating coils for X, Y and Z, is placed beneath the surgical bed. The electromagnets produce monotonically varying magnetic fields, resulting in a known gradient in the three orthogonal directions. Fig. 2. (b) shows the magnetic field gradient in the X-direction. The two devices can simultaneously sense the magnetic field at their respective locations and communicate it wirelessly to an external receiver. The receiver maps the field-data to spatial coordinates, and the relative locations of the devices are then displayed on a computer screen in real time. This can enable the surgical team to maneuver to screw-hole locations without using any X-Ray fluoroscopy [17]. In addition to the 3D position, orientation information of the devices can be critical for certain surgical procedures, such as the one shown in Fig. 2, and is discussed in Section-V. It is also to be noted that the relative position of the hole, with respect to the drill, will be obtained after calibration to compensate for the known location-offset between the hole and the device. If the device-location with respect to anatomical features (like specific bones, muscles or other internal body parts) is desired, which might be valuable for certain surgical applications, it can be obtained by using existing imaging modalities like X-Ray and MRI in conjunction with our system.

III. Wireless Implantable Micro-Device

The wireless and battery-less devices D1 and D2 in Fig. 2 consist of a 3D magnetic sensor, an ASIC (Controller-Chip) designed in 65nm CMOS process, and an inductor-coil wound along the edges of the device. For this prototype device, we have used AK09970N as the 3D magnetic sensor, which communicates with the Chip over the I2C protocol. The sensor is based on Hall-effect, has 16-bit data out for each of the 3-axis magnetic components, high sensitivity (1.1-3.1µT/LSB) and measurement range (± 36mT), and a footprint of 3x3x0.75mm^3. The spatial localization resolution (Δx) obtained by the system, in each of the three dimensions, is given by Eq. (1).

$$\Delta x = \frac{\Delta B_{eff}}{G}\left\{1 + \sqrt{\left(\frac{\delta G_i}{G}\right)^2 + \left(\frac{\delta G_s}{G}\right)^2}\right\} \quad (1)$$

$$\Delta B_{eff} = \sqrt{(\Delta B_i)^2 + (\Delta B_j)^2 + (\Delta B_k)^2} \quad (2)$$

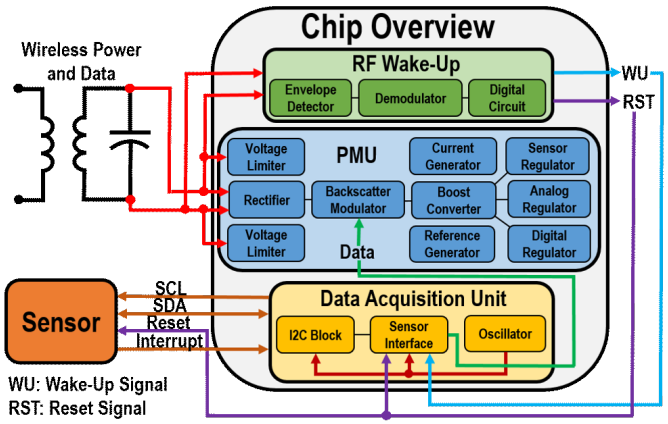

Fig. 3. Complete Controller-Chip overview with block-level description of the circuits inside PMU, RFW and DAU. Detailed circuit-level in [18].

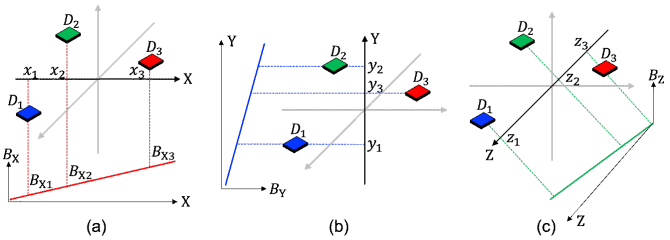

Fig. 4. Conceptual overview of 3D localization of devices $D_1 - D_3$. (a) For the X-direction, a monotonically varying magnetic field is created to result in a field gradient. Each device measures the total field magnitude at its location, which is unique for each point along the X-axis. This process is repeated for localization in (b) Y and (c) Z direction.

ΔB_{eff} is the effective resolution that the sensor can achieve while performing a magnetic field measurement. It is dictated by the noise of the sensing and processing units, the most dominant being the quantization noise. Since the sensor measures three orthogonal components (denoted by i, j, k) of the magnetic field, ΔB_{eff} is composed of the error in each component, as given by Eq. (2). G is the applied magnetic field gradient, which is determined by the current in the electromagnets and their geometrical structure. Two major noise sources have been identified in G: (i) δG_i – error caused by field interpolation; and (ii) δG_s – error caused by variations in supply current. Since δG_i and δG_s are independent and uncorrelated, they add in quadrature. The goal is to keep the contributions by these two error sources below 1% so that RHS in Eq. (1) reduces to $\approx \Delta B_{eff}/G$. With G = 30mT/m and ΔB_{eff} < 3μT, the system can achieve Δx < 100μm, as discussed later in detail.

One of the most important aspects of the device is to be completely wireless, such that it can be hermetically sealed and sterilized to be used with surgical implants inside the body. Wireless operation is achieved through the CMOS Controller-Chip, which is at the core of the implantable device. It performs wireless power and data telemetry at 13.56MHz through the inductor-coil. This eliminates the use of any batteries that might cause lifetime and bio-compatibility issues for a long-term implant. The Chip consists of a Power-Management-Unit (PMU) to convert AC power into regulated DC power and voltage boosting to drive the sensor; an RF Wake-Up (RFW) block to perform wireless data communication; and a Data-Acquisition-Unit (DAU) to interface with the sensor over the I2C protocol. The Chip's top-level architecture is shown in Fig. 3. Detailed description and circuit schematics of the sub-blocks in PMU, RFW and DAU are provided in [18] by the authors.

IV. Magnetic Field Gradient

A simplified view of the magnetic field gradients used for encoding the device location is shown in Fig. 4. Three devices D_1, D_2 and D_3 are located in the FOV. To localize the devices along the X-axis, a monotonically varying magnetic field B_X is generated that has a gradient in its *total magnitude* along the same axis. The gradient ensures that no two points along the axis have the same value of the magnetic field magnitude. This implies that the relationship described by Eq. (3) holds between the magnitude of the field measured by the three devices, denoted by B_{X1}, B_{X2} and B_{X3}, as shown in Fig. 4. (a). The three orthogonal components of the field ($\hat{x}B_X, \hat{y}B_X, \hat{z}B_X$) measured by each device, are used for computing the field magnitude at the device's location, as described in Eq. (4).

$$\|B_{X1}\| < \|B_{X2}\| < \|B_{X3}\| \tag{3}$$

$$\left\|B_{Xi,\ i=1,2,3}\right\| = \sqrt{(\hat{x}B_{Xi})^2 + (\hat{y}B_{Xi})^2 + (\hat{z}B_{Xi})^2} \tag{4}$$

For the X-dimension, since the magnetic field B_X has a net gradient in its magnitude along the X-axis, G_X is defined as the derivative of $\|B_X\|$ with respect to x, as given by Eq. (5).

$$\text{X} - \text{Gradient} = G_X = \partial\|B_X\|/\partial x \tag{5}$$

Similarly, to localize the devices along the Y and Z axis, a monotonically varying magnetic field is generated that has a gradient along the same axis, and the corresponding field magnitude is measured by the devices (Fig. 4). Using the field measurements along the three orthogonal axes, the complete 3D position of all the devices can be decoded unambiguously. Since the gradient manifests in the *magnitude of the magnetic field* along each axis, this localization technique is immune to potential inaccuracies caused by device misalignment and orientation mismatch relative to any specific coordinate system. As the orientation changes, the measured individual field components might change from those in Eq. (4), but the overall magnitude remains the same, thus reinforcing Eq. (3). This is also evident from Eq. (2), as the sensor may have its relative coordinates of $\hat{\imath}, \hat{\jmath}, \hat{k}$ different from the $\hat{x}, \hat{y}, \hat{z}$ in Eq. (4), but the magnitude remains unchanged.

A. Gradient Coils Design Specifications

The gradient required along each axis is described by Eq. (5). Special emphasis needs to be paid to the magnitude function since it implies that all three orthogonal components of the vector field contribute to the gradient. It would be ideal to have a single field polarization, suitably in $\hat{z}$, that could produce a field gradient along the required axis of either X, Y or Z. However, such a field is not a solution of Maxwell's equations

and thus cannot be produced by a real field-generator. The problem is compounded by the flatness requirement of the field-generator, which rules out volume-enclosing architectures used in closed-bore cylindrical MRI scanners. Summarizing all the crucial specifications governing the design of our electro-magnetic gradient coils: (i) completely planar coils that can easily slide beneath the patient's bed to ensure no inhibition to the surgeon's movement from the top; (ii) enhanced FOV to allow sufficient room for surgical navigation and alignment; (iii) high gradient strength G to achieve high resolution; (iv) high current efficiency to make the maximum use of current drawn by the gradient coils; (v) low coil-length to have less inductance (for fast switching) and less resistance (for lower heating); and (vi) absence of bulky permanent magnets producing a strong magnetic field, due to their incompatibility and safety issues with nearby metals [19][20].

The gradient coil efficiency η is defined as the ratio of the magnetic field gradient (G) produced by the coil to the current drawn (I). To study and confirm the magnetic field profiles and the gradients generated by the coils, static magnetic field simulations were carried out in a magneto-static software Radia. The geometrical design parameters of the coils were also optimized in Radia. The target FOV was initially set to be 15x15x10cm^3. The value of G discussed in the following sections is the average value, in order to keep the DC current selection straightforward. The magnetic field notations used in this work are described below. Field vectors generated by each coil with their components along the three orthogonal axes:

$$\begin{matrix}\mathrm{X-Coil}\\ \mathrm{Y-Coil}\\ \mathrm{Z-Coil}\end{matrix} = \begin{bmatrix}B_\mathrm{X}\\ B_\mathrm{Y}\\ B_\mathrm{Z}\end{bmatrix} = \begin{bmatrix}\hat{x}B_\mathrm{X} & \hat{y}B_\mathrm{X} & \hat{z}B_\mathrm{X}\\ \hat{x}B_\mathrm{Y} & \hat{y}B_\mathrm{Y} & \hat{z}B_\mathrm{Y}\\ \hat{x}B_\mathrm{Z} & \hat{y}B_\mathrm{Z} & \hat{z}B_\mathrm{Z}\end{bmatrix} \quad (6)$$

X-Coil's (similarly others) field plotted along different axes:

$$\begin{bmatrix}\hat{x}B_{\mathrm{X}(x)} & \hat{x}B_{\mathrm{X}(y)} & \hat{x}B_{\mathrm{X}(z)}\\ \hat{y}B_{\mathrm{X}(x)} & \hat{y}B_{\mathrm{X}(y)} & \hat{y}B_{\mathrm{X}(z)}\\ \hat{z}B_{\mathrm{X}(x)} & \hat{z}B_{\mathrm{X}(y)} & \hat{z}B_{\mathrm{X}(z)}\end{bmatrix} \quad (7)$$

Where $\hat{z}B_{X(y)}$ denotes the Z-component of the X-Coil's vector field B_X, plotted along the Y-axis.

B. Z-gradient Coil

The generation of Z gradient is relatively simpler than that of X and Y. This is because the magnetic field strength produced by a coil decreases monotonically as the distance from the surface is increased, irrespective of the coil geometry. Hence, to create a Z-axis gradient in the magnetic field magnitude, a planar circular coil carrying current in a counter-clockwise direction suffices, as shown in Fig. 5 (a). The center of the coil produces a magnetic field pointing upward. The field magnitude ($\|B_Z\|$) thus generated along the Z-axis is plotted in Fig. 5 (b) for varying values of X at Y=0. Since the coil is symmetric about X and Y, an identical plot is obtained while varying the Y-coordinate at X=0. The 10cm Z-FOV is plotted from 1cm above the coil surface, to a height of 11cm. The

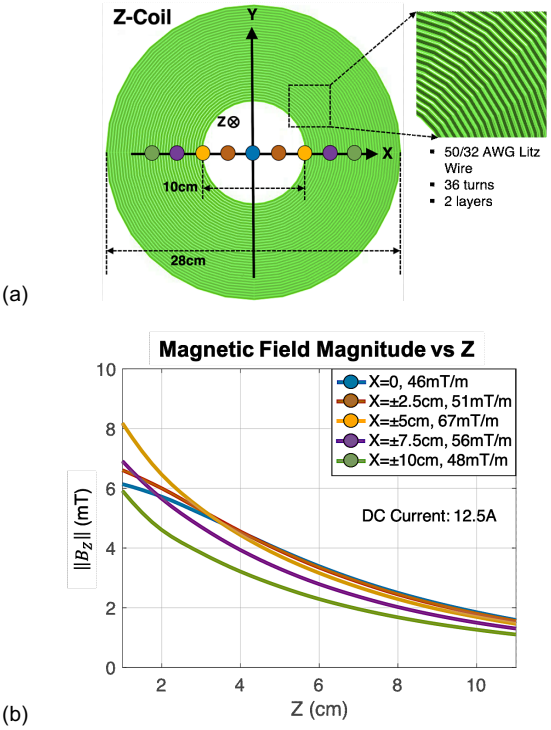

Fig. 5. (a) Z-Coil. (b) Measured magnetic field magnitude $\|B_Z\|$ along the Z-axis, plotted for different values of X (at Y=0).

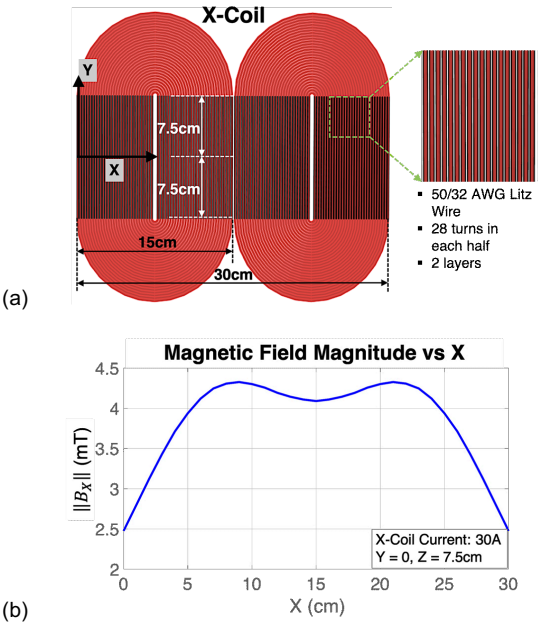

Fig. 6. (a) X-Coil consisting of two spirals placed next to each other. (b) Measured magnetic field magnitude $\|B_X\|$ along the X-axis.

gradient strength G is 46mT/m at X=0, reaches a maximum of 67mT/m at X=±5cm, and comes down to 48mT/m at X=±10cm, thus ensuring G > 30mT/m over a span of 20cm along the X-axis (same along the Y-axis). The DC current used in the Z-Coil is 12.5A, which results in an average value of η to be 4.3mT/m/A. The 10cm cavity at the center of the Z-Coil is

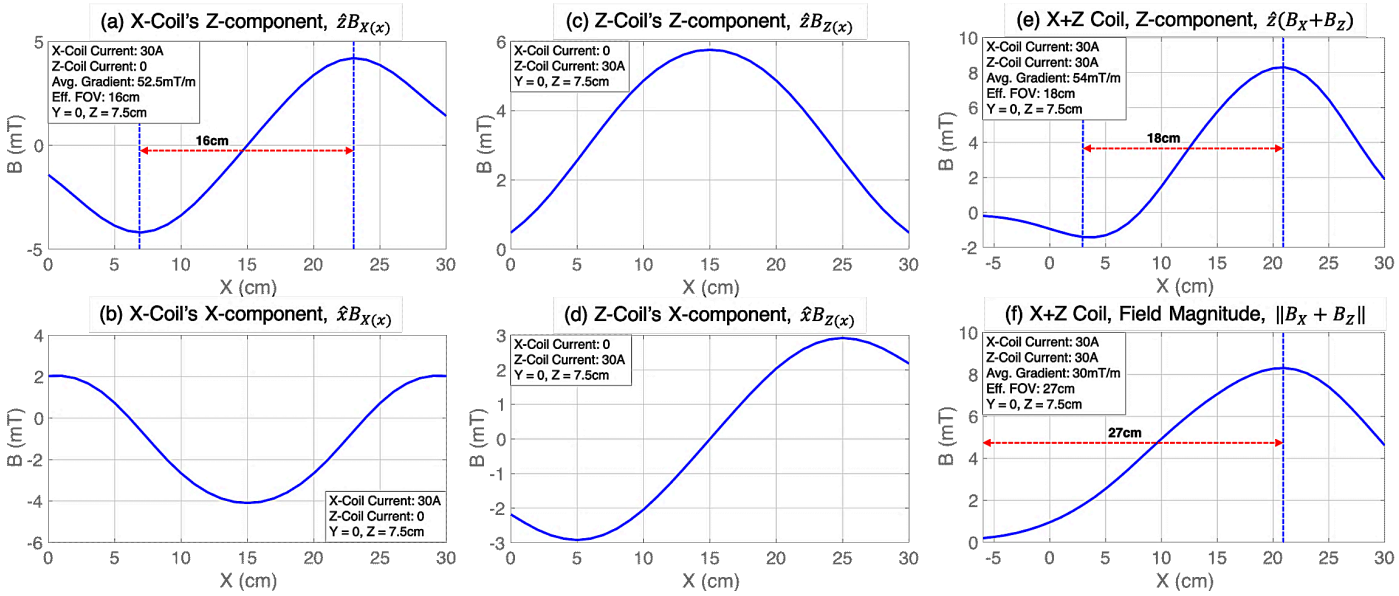

Fig. 7. (a) Simulated Z-component and (b) X-component of X-Coil's magnetic field along the X-axis. (c) Z-component and (d) X-component of Z-Coil's magnetic field plotted along the X-axis. (e) Z-component and (f) complete magnetic field magnitude when both X and Z coils are on together.

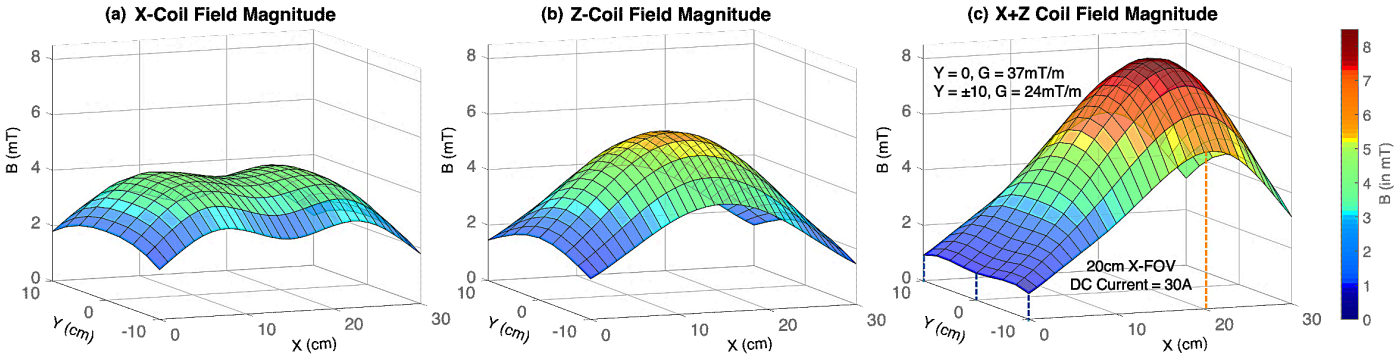

Fig. 8. Measured magnetic field magnitude when (a) only X-Coil is on, (b) only Z-Coil is on, and (c) both X and Z coils are on simultaneously. The Y-coordinate is varied from -10 to 10cm with Z=7.5cm. Gradient *G* in (c) attains the highest value at Y=0 (center) and gradually decreases at Y=±10cm.

particularly important when the coil's field is used for enhancing the X and Y gradients' FOV, as discussed in the following section. It also enhances the linearity of the Z-Coil's field magnitude, which is more exponential in the absence of the cavity.

C. X-gradient Coil

In order to create a gradient in the magnetic field along the X-direction using planar electromagnetic coils, the most common technique is to place two identical coils, carrying currents in opposite directions, right next to each other [21]. The prototype X-Coil designed in this work is shown in Fig. 6 (a). The physical coil-span should be higher than or equal to the required FOV of 15cm, which is the reason for designing the coil with a 30cm span along the X-axis. The clockwise current-carrying half (left) produces a magnetic field B_X that has a Z-component ($\hat{z}B_X$) pointing into the plane, denoted by negative values. The counter-clockwise current-carrying half (right) produces $\hat{z}B_X$ pointing out of the plane, denoted by positive values. This creates a monotonically varying Z-component in B_X along the X-axis, i.e. $\hat{z}B_{X(x)}$, between the centers of the two coils, as shown in Fig. 7 (a). The elongation of the two spirals of the X-Coil is kept to be 15cm so as to keep the X-gradient homogenous across the required Y-FOV. The Y-Coil is designed identically to X, but rotated by 90° to align the gradient along the Y-axis.

Generating a gradient in the Z-component of B_X is not sufficient for the localization shown in Fig. 4. As described by Eq. (3) - (5), the *magnitude* of the magnetic field needs to be monotonically varying, which implies that the gradient should manifest in $\|B_X\|$. Fig. 6 (b) shows $\|B_X\|$ generated by the X-Coil and plotted along the X-axis. The highly non-linear nature of this plot is due to the following reasons: (a) the addition of non-zero and non-linear X and Y components ($\hat{x}B_X$ and $\hat{y}B_X$) to $\hat{z}B_X$, (b) non-linearity of the magnitude function, which flips the negative half of the field to result in an even-function centered at X=15cm. In order to circumvent this problem, one possible solution, as employed in MRI, is to have a significantly higher static background field B_0, which points in the Z-direction. Using $B_0 \geq 0.5$T, it is observed that $\|B_X\|$ is

dominated by $\hat{z}B_X$ and the field profile closely resembles Fig. 7 (a). The high value of B_0 is necessary to suppress the contributions from the non-linear and undesirable $\hat{x}B_X$ and $\hat{y}B_X$, and to provide a high positive offset to $\hat{z}B_X$ which can accentuate its value in the field magnitude plot. However, generating B_0 of such a high value defeats the purpose of this work since it requires either a strong and bulky permanent magnet, or electromagnets carrying very high DC currents. We employ a different technique, described in the following section, for creating the required gradient in $\|B_X\|$ along the X-axis, while achieving a sufficiently high X-FOV.

D. X and Y FOV Enhancement

The non-zero magnetic field components of the X-Coil along the X-axis (at Y=0, Z=7.5cm), denoted by $\hat{z}B_{X(x)}$ and $\hat{x}B_{X(x)}$, are shown in Fig. 7 (a) and (b) respectively. Combining these two gives a highly non-linear magnitude plot for $\|B_X\|$, as was shown in Fig. 6 (b). The Z-Coil's field is then evaluated in more detail. The non-zero magnetic field components produced by the Z-Coil along the X-axis (at Y=0, Z=7.5cm), are $\hat{z}B_{Z(x)}$ and $\hat{x}B_{Z(x)}$, as shown in Fig. 7 (c) and (d) respectively. The strictly positive and monotonic nature in either half of $\hat{z}B_{Z(x)}$ makes it an appropriate candidate for offsetting the negative half of $\hat{z}B_{X(x)}$. Additionally, $\hat{x}B_{Z(x)}$ exhibits a highly linear behavior from 5cm to 25cm, the predominant region of non-linearity in $\hat{x}B_{X(x)}$, indicating that a superposition of the two would be relatively more linear than the latter alone.

The Z-Coil is then positioned right beneath the X-Coil and both are turned on simultaneously. The resulting magnetic field profile along the X-axis is plotted in Fig. 7 (e) and (f). Fig. 7 (f) highlights that the magnitude of the resultant magnetic field produced by the coil combination, when plotted along the X-axis, is strictly positive *and* monotonic from -6cm to 21cm, generating an effective FOV of 27cm and displaying high linearity. The negative position coordinates simply imply that the region is beyond the physical location of the coils. Compared to the physical horizontal-span of the X-Coil (30cm), the X-FOV measures 27cm with this new combination, yielding an effectively useful coil-span of 90%. For off-center regions where Y≠0, the Y-component of the X and Z coils is also present and contributes to the magnitude of the field generated by the two coils. Nonetheless, the qualitative nature of the field profile resembles Fig. 7 (f) in all the cases, as discussed below.

E. Gradient Variation in FOV

To evaluate the homogeneity of the X-gradient resulting from employing both the X and Z coils in tandem, the gradient profile is studied for a varying range of Y-coordinates. In Fig. 8 (a), the field magnitude generated by only the X-Coil is plotted along the X-axis, while varying Y from -10 to 10cm and keeping Z=7.5cm. Next, in Fig. 8 (b), the field magnitude generated by only the Z-Coil is plotted along the X-axis, while varying Y from -10 to 10cm and keeping Z=7.5cm. Due to the circular nature of the Z-Coil, its field magnitude (along X-axis) is non-homogenous across Y-coordinates, with the center (Y=0) having the highest field gradient that gradually falls as Y is increased to ±10cm. This effect also manifests in the field profile when both the coils are turned on simultaneously, the magnitude of which is plotted in Fig. 8 (c) for Y from -10 to 10cm and Z=7.5cm. The gradient G reduces monotonically from 37mT/m at Y=0 to 24mT/m at Y=±10cm, while maintaining a 20cm X-FOV throughout. Similarly, the value of G reduces monotonically as the Z-coordinate is increased (57mT/m at Z=5cm, Y=0, to 23mT/m at Z=10cm, Y=0), which is expected because the field strength falls as the height from the coil-surface is increased, irrespective of the coil-geometry.

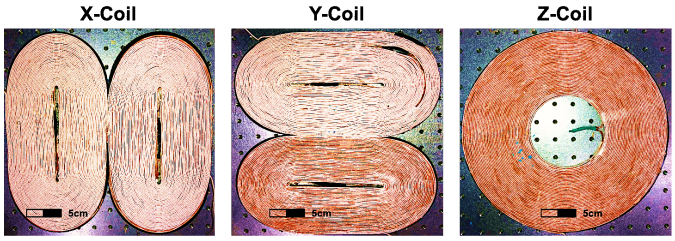

Fig. 9. Fully assembled X, Y and Z coils using 50/32 AWG Litz wire.

TABLE I
GRADIENT COIL SPECIFICATIONS

Parameter	Z Coil	X & Y Coils
FOV Used	10cm	20cm
DC Current	12.5A	30A
Avg. η	4.3mT/m/A	588μT/m/A
Inductance	1.64mH	1.5mH
Resistance	1Ω	950mΩ

This implies that for a given sensor resolution in Eq. (1), the obtained position resolution would be higher as the devices move closer to the center of the FOV spanning 20x20x10cm^3 in X, Y and Z respectively, as the gradient G is higher in the center-region. To improve the position resolution obtained at the boundary planes of the FOV, either the DC current in coils should be increased (resulting in a stronger gradient), or the sensor resolution should be higher. Keeping the maximum current as 30A in this work, we employ the sensor in low-noise mode towards the boundary planes where the gradient strength is <30mT/m. In the low-noise mode, the sensor has a resolution of 1μT, requiring only 10mT/m to achieve 100μm of position error. However, the current consumption in low-noise mode is 2.2mA for 850μs, compared to 1.5mA for 250μs in the low-power mode (3μT). With the extra power penalty on the sensor side, the desired position resolution of 100μm can be achieved in the entire FOV. This is the primary reason for designing the PMU and other circuit blocks in the Controller-Chip with very high efficiency – to wirelessly send comparatively higher power to the sensor when operated in the low-noise mode.

Extending the same principle to Y-gradient, both the Y and Z-Coils are turned on simultaneously for a monotonic Y-FOV. Similar to X, this also leads to a 27cm long Y-FOV with a highly homogenous, monotonic and linear magnetic field profile. Since the 30A of DC current is sufficient to ensure a gradient strength of ≥10mT/m at all the boundary planes of a 20x20x10cm^3 volume, we restrict the FOV to points inside this

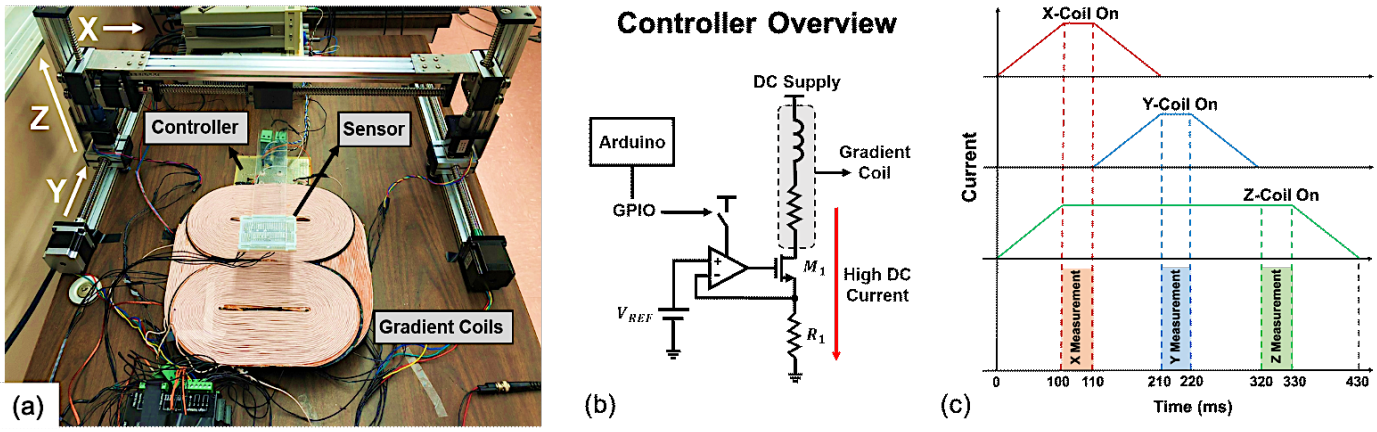

Fig. 10. (a) Automated 3D-stage consisting of X, Y and Z actuators for characterizing the FOV of gradient coils. (b) Schematic overview of the controller-board used for driving the coils. (c) Global timing diagram of the gradient coil on/off time-instants along with the field-measurement phases.

volume. Each point inside the FOV corresponds to a unique set of magnetic field values obtained from the three orthogonal gradients, as summarized by the following equations:

Magnetic field during X-gradient (X + Z-Coil On):

$$\|B_X + B_Z\| = \sqrt{(\hat{x}B_X + \hat{x}B_Z)^2 + (\hat{y}B_X + \hat{y}B_Z)^2 + (\hat{z}B_X + \hat{z}B_Z)^2} \quad (8)$$

Magnetic field during Y-gradient (Y + Z-Coil On):

$$\|B_Y + B_Z\| = \sqrt{(\hat{x}B_Y + \hat{x}B_Z)^2 + (\hat{y}B_Y + \hat{y}B_Z)^2 + (\hat{z}B_Y + \hat{z}B_Z)^2} \quad (9)$$

Magnetic field during Z-gradient (Z-Coil On):

$$\|B_Z\| = \sqrt{(\hat{x}B_Z)^2 + (\hat{y}B_Z)^2 + (\hat{z}B_Z)^2} \quad (10)$$

Another advantage of this technique is the utilization of the X and Y components of the magnetic field produced by the X and Z coils, as seen in Fig. 7. The magnetic field magnitude plotted in Fig. 7 (f) consists of contributions from the X and Y components as well, which are otherwise non-desirable and eventually wasted in MRI. Hence, our technique leverages the gradient coils to their maximum utilization by using *all* the field components produced by the X and Z coils, to yield a ≥ 90% usable FOV without using any additional resources.

F. Gradient Coils Assembly

The three gradient coils are assembled using a 50 stranded, 32 AWG Litz wire (50/32). Single-stranded equivalent AWG wires are not an appropriate choice here because of – (i) their mechanical rigidity, which makes them difficult to be cast into circular coils; and (ii) their increased resistance at high frequencies (during gradient switching) due to skin-effect. These factors make multi-stranded Litz wire an appropriate choice for the coils. The Z-Coil consists of 2 layers, each with 36 turns. Each elongated half of the X and Y coils consists of 2 layers, with 28 turns/layer. Fig. 9 shows the fully assembled coils and Table-I lists their individual parameters. Finally, the three coils are stacked together concentrically to give a single planar structure with the X-Coil on top, Y-Coil in the middle, and Z-Coil on the bottom. The complete coil-stack measures 30x30x1cm^3.

For applications requiring bigger FOV, the physical dimensions can be correspondingly scaled for all the coils. More layers can be added to generate a proportionately higher FOV and/or gradient since the plots in Fig. 5 to Fig. 8 correspond to only two layers of windings for each of the coils. The DC current is another parameter for scaling the FOV vertically. With a DC current of 30A in both the X and Z coils, the average value of η for the X-gradient is 588μT/m/A. Heating of the coils is discussed in the following sub-section G. The field magnitudes plotted in Fig. 5, Fig. 6 and Fig. 8 are all measured values during the characterization phase described in the sub-section G. Fig. 7 consists of simulated plots in Radia to show the individual components of the field and the intuition behind combining them in a specific order. The simulated and measured field profiles have an excellent agreement (<1% error).

G. Gradient Characterization in FOV

The FOV above the coil surface needs to be characterized by measuring magnetic field values and storing them in a lookup table (LUT), such that they can be retrieved for position decoding after measurements by the device. For robotically wound coils with consistent spacing between the turns, it is possible to model them accurately in Radia. Thereafter, the magnetic field at 100μm (or lower) increments in the 20x20x10 cm^3 FOV can be measured by simulations in Radia and stored in the LUT. The increment step should be at least equal to or less than the desired value of Δx in Eq. (1), to ensure that the error is not limited by characterization. However, the increments cannot be arbitrarily small since they require a proportionately higher simulation time. With 100μm increments, the estimated simulation time on a high-performance server for completely characterizing the current FOV is less than a few hours. Also, this needs to be performed *only once* for a given set of coils since the magnetic field values for an arbitrary DC current can be obtained by linearly scaling the field values stored in the LUT.

Since the prototype coils developed in this work are hand-wound, the undesirable minute gaps between the turns are not

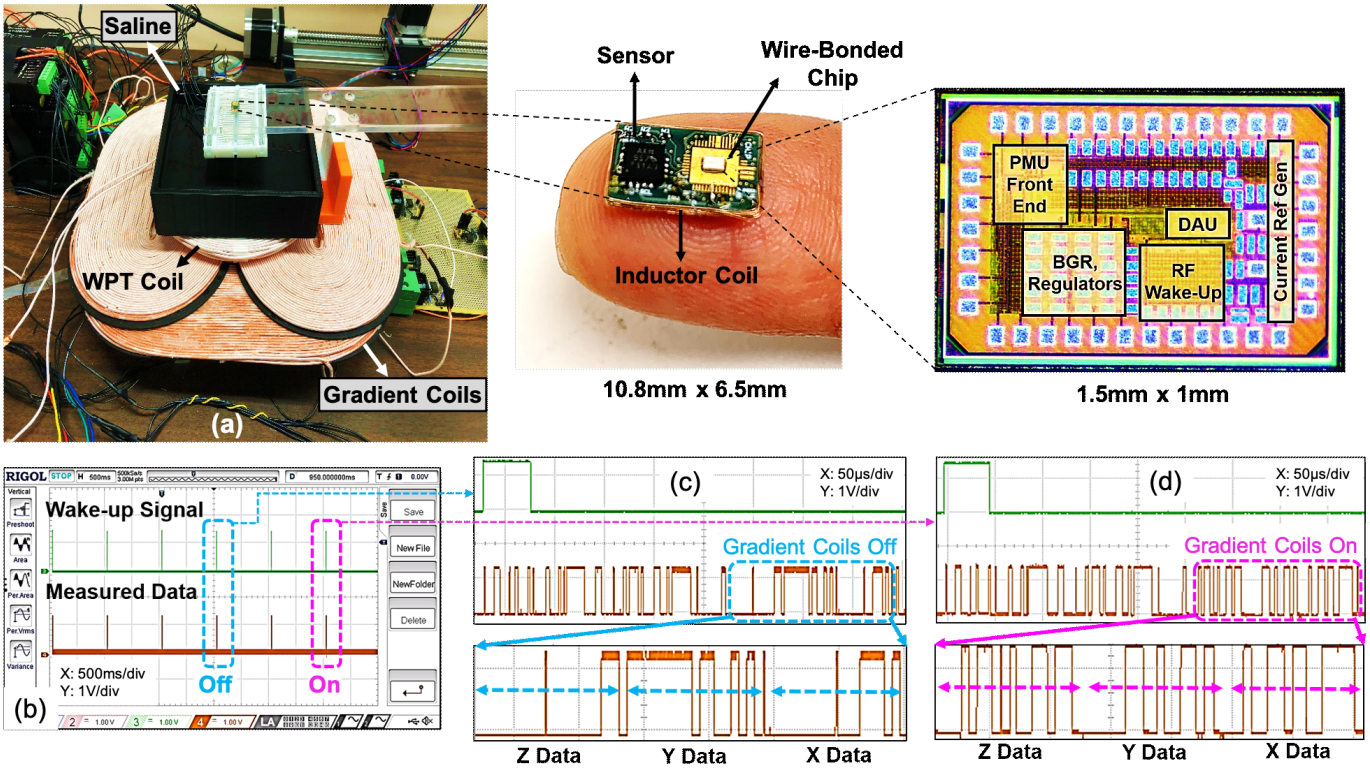

Fig. 11. (a) Measurement setup for localization consisting of the completely assembled device and the magnetic field gradient coils. Controller-Chip (65nm CMOS) micrograph is also shown. (b) Decoded wake-up signal and the measured digital data stream. (c) Zoomed signals when gradient coils are off and earth's ambient magnetic field is measured by the Chip. (d) Measured magnetic field values when the gradient coils are on.

exactly consistent, thus making it difficult to accurately model the coils in Radia. As a result, the coils were characterized externally by the setup shown in Fig. 10 (a) since the required resolution of 100µm cannot be achieved using the Radia-based characterization for these coils. The setup comprises linear actuators that move in the X, Y and Z directions and measure the magnetic field at every 2.5mm step. Points in between the 2.5mm steps are interpolated using Makima, a piecewise cubic Hermite interpolation in MATLAB. This results in an ultra-finely characterized FOV with steps of 10µm in X, Y and Z, such that the interpolation error of δG_i described in Eq. (1), causes <1% variation in G. An increase in the step size from 2.5mm causes δG_i to increase proportionately. The 3D magnetic sensor (AK09970N) is mounted on a fiberglass arm and makes a field measurement at every position step. Arduino is used as the global micro-controller to simultaneously control the movement of the actuators and interfacing with the sensor. To reduce the effect of the sensor noise from 15µT_{pp} (measured in the lab) to ≤ 1µT_{PP}, the sensor averages 200 measurements at each location. The earth's ambient magnetic field is also measured at each location and subtracted from the gradient coil's field. The corrected field values are then stored in the LUT. Each step consisting of all the measurements and the movement of the actuators takes <10s, requiring 15days to completely characterize the 20x20x10cm^3 FOV with 2.5mm increments. For future versions of the coils that are robotically assembled, the total time for characterization can be reduced significantly using Radia.

It is crucial to have a constant DC current from the power supply into the coils, i.e. minimize δG_s in Eq. (1), since variations in current cause field-offsets that directly translate to position error. Therefore, a controller-board is designed to precisely control the DC current into the gradient coils so as to get $\delta G_s \approx 0$. A high-level schematic of the board is shown in Fig. 10 (b). V_{REF} and R_1 together set the value of the DC current since $I_{DC} = V_{REF}/R_1$. An N-channel MOSFET driver M_1 (PSMN2R7-30PL) rated for 100A is used for handling the high DC current coming into the coils. R_1 is chosen with high temperature stability (MP930-0.020-5%) to ensure a thermally stable current value. All of these steps ensure that the contributions from δG_i and δG_s in Eq. (1) are kept ≤1%.

The global timing diagram is shown in Fig. 10 (c). Measurement phases are synchronized to occur during the 10ms time-window when the DC currents in the coils are stable. The 10ms span is sufficient for the 25 measurements that are performed during the normal operation of the device, as will be discussed in the following section. Since the number of measurements at each step during the characterization phase are much higher, a 100ms span is required instead. The relatively high ramp-up/down time of 100ms is primarily due to the DC current supplies used for this application, which limits the number of measurements to 7 in 1s. The high rise/fall time also causes 85% of the total power dissipated as heat, and only 15% is contributed by the 10ms measurement time-window for each of the X, Y and Z measurements shown in Fig. 10 (c). The use of high-efficiency DC supplies like [22]-[23] can reduce the

heat loss by almost 80% by significantly reducing the high rise/fall times. The entire duty-cycled operation of the coils, shown in Fig. 10. (c), results in ≈300W of average power lost as heat with the current DC supplies. For continuous localization carried out over 1 minute, this produces 18kJ of energy in the coils, resulting in 3.4^{0}C rise in the surface temperature. For procedures requiring a longer localization time, cooling pads or thermal insulators may be used above and below the coils to dissipate the heat faster.

A more energy-efficient approach for designing future versions of the gradient coils with larger FOV would be to use more layers of windings (instead of two used in the first prototype here), rather than increasing the DC current that has square-dependence on heat-loss (I^2R). The former approach increases the heat linearly and also provides a larger coil volume for heat dissipation. The extra layers will increase the thickness of the coil-stack, which is not a problem since the stack is completely planar and can easily slide beneath the surgical bed. For the switching speed, it can be seen from Table I that the L/R time constant for X and Y Coils is 1.58ms and for Z-Coil is 1.64ms. Both of these are significantly less than the 100ms rise/fall times of the DC supply and therefore have a negligible effect on switching speed.

V. Measurement Results

The complete measurement setup for the localization system is shown in Fig. 11 (a). The magnetic field gradient coil stack is placed on the bottom with the primary wireless power transfer (WPT) inductor-coil on top. A 5cm high saline tank separates the device from the WPT coil. The device consisting of the Silicon-Chip, 3D magnetic sensor, inductor-coil and FR4 PCB, is completely bio-compatible. When the device is used as an actual implant in a surgical space, it would need to be encapsulated by poly-dimethyl siloxane (PDMS) and sealed hermetically [24]. The device functionality is unaffected by such encapsulation. After wirelessly powering up the Chip, a wake-up signal is sent to trigger magnetic field measurement by the sensor. The decoded wake-up pulses are shown in Fig. 11 (b). These are synchronized with the gradient on/off signal to allow high DC current in the coils only during the measurement phase. The sensor generates a 16-bit digital data stream for each of the X, Y and Z components of the field. Fig. 11 (c) shows the zoomed measurement when the gradient coils are off, thus making the Chip measure the earth's magnetic field (±30μT to ±60μT), so as to cancel its effect from the gradient coil's field. The first 8 bits of all the vectors are either 0 or 1, indicating a very small value. The field vectors have significantly higher and strictly positive values, as shown in Fig. 11 (d), once the gradient coils are turned on. After the Chip finishes a measurement, the data is backscattered wirelessly at 100kHz, requiring <1ms for transmission to the external reader module. Offset cancellation and position decoding take <10ms, causing the total latency between the field measurement and position-display to be ≈10ms. However, this gives only one coordinate position and in order to decode the X, Y and Z position, there is an extra 100ms of wait time due to the rise/fall time requirement

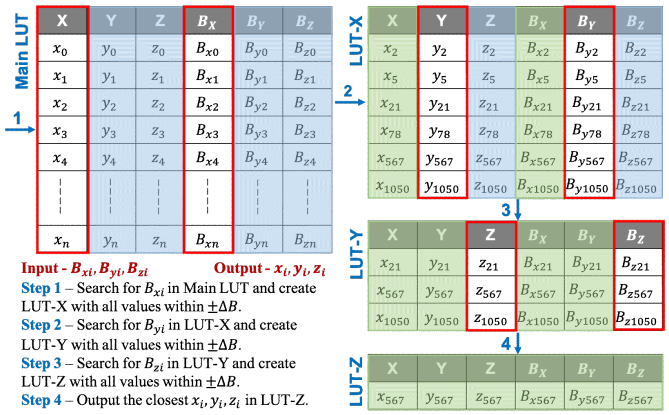

Fig. 12. Overview of the 3D Search-Algorithm for position decoding from the magnetic field values measured by the device in Fig. 11.

of the DC current in the gradient coils, as was shown in Fig. 10 (c). The rise/fall time constraint can be relaxed with the use of more efficient DC supplies [22]-[23] such that the overall latency for a 3D position update is <50ms, with 10ms each for the X, Y and Z measurements, 10ms for decoding and the remaining 10ms for rise/fall time overhead. The latency can be further reduced by decreasing the number of measurements from 25 (which require 10ms for each coordinate) to a single measurement, at the cost of ≤500μm of 3D position error.

Three points in the gradient coils' FOV are chosen, corresponding to three distinct spatial coordinates: (i) X1, Y1, Z1 in the region with G=50mT/m; (ii) X2, Y2, Z2 in the region with G=30mT/m; and (iii) X3, Y3, Z3 in the region with G=10mT/m. The demodulated field values measured at each point, denoted by B_{xi}, B_{yi}, B_{zi}, are given as input to the 3D Search-Algorithm implemented in MATLAB, which outputs the corresponding closest position coordinate (Fig. 12). In Step 1, B_{xi} is compared with all the magnetic field magnitudes stored in the B_X column of the Main-LUT (created during the characterization phase) and a smaller LUT-X is created dynamically that contains all entries of the Main-LUT within $\pm\Delta B$ of B_{xi}. ΔB is chosen to be 100μT to ensure high accuracy by eliminating all false positives. Since B_{xi} corresponds to a large number of B_X values located in the 3D volume above the coil surface, there is more than one row in LUT-X. In Step 2, a similar process is repeated for B_Y using B_{yi}. The intersection of the B_{xi} and B_{yi} planes results in an array of points spread across various planes parallel to the coil surface. B_{zi} is used for the search in Step 3 and finally, the output coordinates are the x_i, y_i, z_i (shown as the 567th entry in Fig. 12) from LUT-Z that correspond to magnetic field values having the smallest Euclidean difference from B_{xi}, B_{yi}, B_{zi}.

The actual position of the Chip, measured from a global reference point on the gradient coils, is known precisely since it is placed on the robotic micro-positioner. The predicted position is the output of the Search-Algorithm discussed above and is also referenced to the same global point on the coils. The error is defined as the difference between the actual and the predicted position and is plotted against the number of

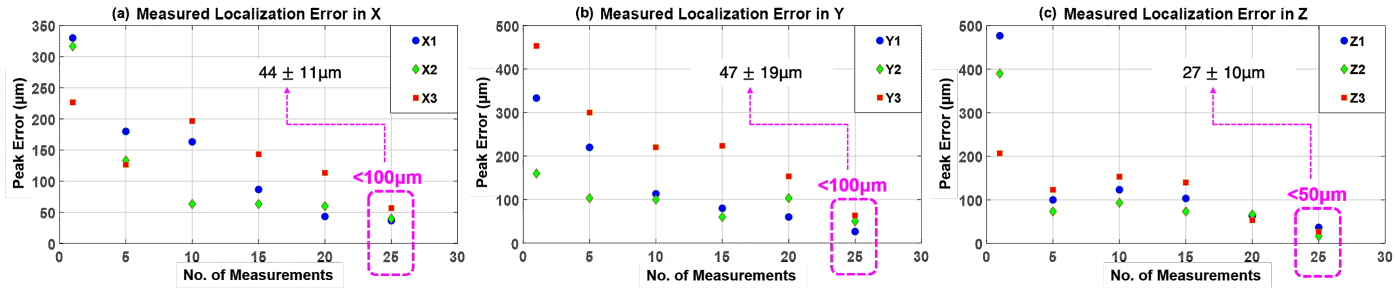

Fig. 13. Measured localization error for (a) X, (b) Y, and (c) Z direction. Peak error, which is the difference between the predicted position (output of the Search-Algorithm) and the actual position (measured from a global reference point on the gradient coils), is plotted vs the number of measurements averaged. An ensemble of ≥25 measurements is averaged at each position to get the peak error of <100µm in all three dimensions.

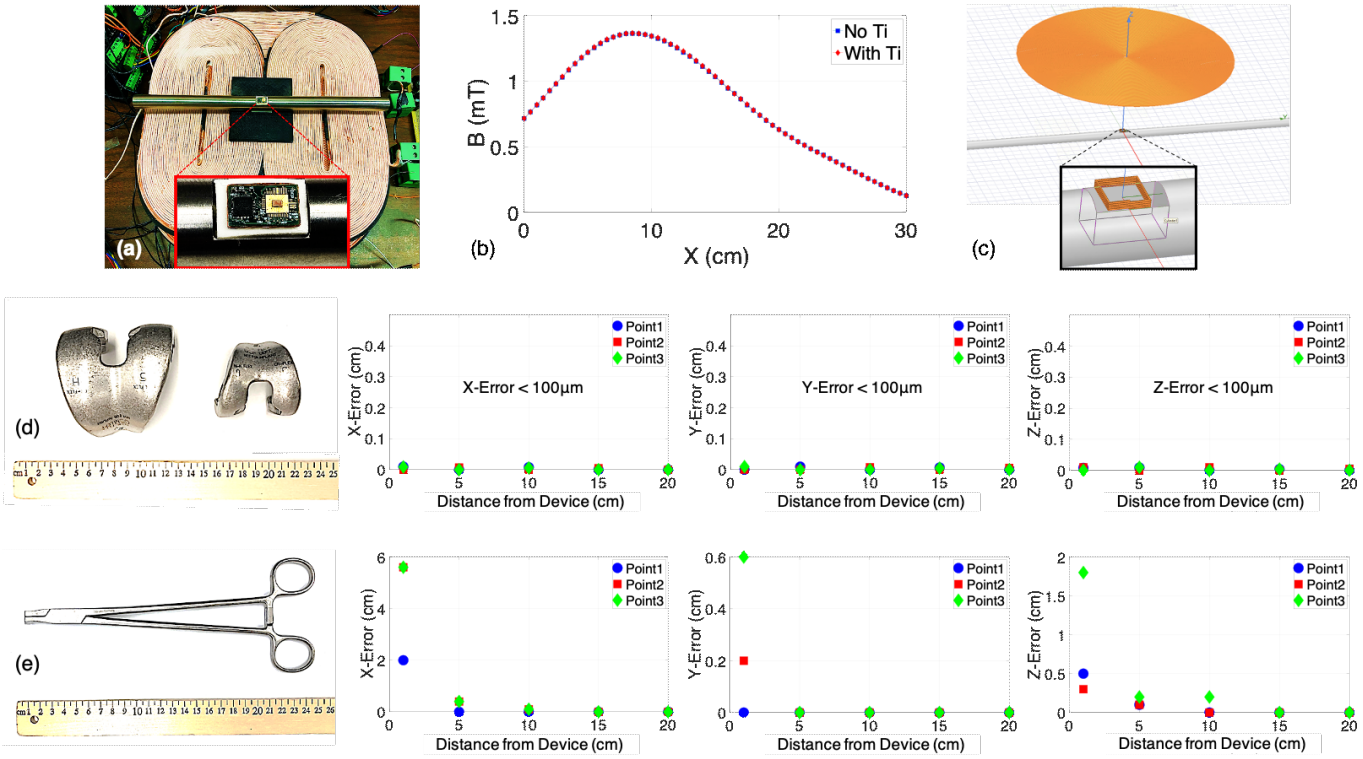

Fig. 14. (a) Measurement setup in the presence of Ti rod, with the device placed on top of a PDMS-filled cavity. (b) Lack of field distortion in the presence of Ti. (c) Simulation setup in HFSS to determine the cavity-depth. (d) Non-magnetic surgical implant used for studying the effect of interference. Peak error in the decoded position (at 3 different points) is plotted for X, Y and Z as the distance of the implant from the device is varied. (e) Same experiment is performed for a magnetic surgical tool, where the error goes to <100µm when the tool is ≥15cm away from the device.

measurements (taken at the same position) in Fig. 13. The accuracy is defined qualitatively as the inverse of the error and therefore, a smaller error implies a larger accuracy. In the high gradient regions (≥30mT/m), the sensor is operated in low-power mode which has a sensitivity of 3µT/LSB. Given the error due to δG_s and δG_i is ≤1%, this should ideally produce a peak error of <100µm, as per Eq. (1). However, the error plots in Fig. 13 show that the peak position error from a single measurement can be 500µm. This is attributed to the random noise of the sensor, which has a peak measured value of 15µT. To mitigate the effect of sensor noise on the position error, averaging of several measurements is performed for a given position. As seen from the plots in Fig. 13, with increasing the number of measurements, the peak error gradually decreases. It is found that with averaging an ensemble of ≥25 measurements, the peak error reduces to <100µm. The averaging window can be relaxed for: (i) a sensor with higher sensitivity and lower noise, thus reducing ΔB_{eff} in Eq. (1); and/or (ii) higher field gradient to increase G. In the low gradient region (G<30mT/m), the sensor is operated in the low-noise mode, achieving a sensitivity of 1µT/LSB that results in <100µm of position error. Thus, by selectively operating the sensor in low-power or low-noise mode, the desired error threshold of 100µm is maintained in the entire FOV. The mean and std. deviation of the error obtained at the three different points (with averaging 25 measurements) shown in Fig. 13 is: (i) X: 44 ± 11µm, (ii) Y: 47 ± 19µm, and (iii) Z: 27 ± 10µm. Note that such a high resolution is necessary only when the surgeon is very close to the screw-hole, and can be relaxed during the initial maneuvering to quickly navigate to the approximate hole

TABLE II
PERFORMANCE SUMMARY AND COMPARISON – SYSTEM LEVEL AND DEVICE LEVEL

System Specifications	This work	TMI 2020 [12]	TMI 2019 [11]	SIGCOMM 2018 [9]	Nat. BME 2017 [16]	TMI 2017 [10]	ASME 2016 [30]	TBME 2013 [13]	US Patent 2003 [31]
Localization Dimension	3D	3D	3D	3D	2D	3D	5D *	3D	6D *
Localization Resolution	100µm	600µm	2.8mm	1.4cm	500µm	2.23mm	2.1mm	1.5-4.44mm	2mm
Localization Modality	Magnetic Field Gradient	Radioactive & Fluorescence	Optical & Ultrasound	RF-based Backscatter	MRI Inspired	Ultrasound & Filtering	Magnetic Tracking	Laser & Conoprobe	MRI Gradients
Sample Rate	7Hz	17mHz	1Hz	N.R.	N.R.	N.R.	200Hz	30Hz	16Hz
Penetration Depth	10cm	2cm **	N.R.	8cm	1.2cm	N.R.	5cm	N.R.	Sensor dependent *#
Field of View	20cm x 20cm x 10cm #	14cm x 14cm x 2cm	24cm x 30cm x 8cm	8cm ##	1.2cm $	16.5cm x 22cm $$	7cm x 7cm x 5cm	N.R.	30cm from center

Device Specifications	This work	SIGCOMM 2018 [9]	Nat. BME 2017 [16]	US Patent 2003 [31]
CMOS Technology	Yes (65nm)	No	Yes (180nm)	No
Wireless Power	Yes	Yes	No	No
Wireless Data	Yes	Yes	Yes	No
Frequency	13.56MHz	830, 870MHz	500MHz #$	N/A
CMOS Chip Area	1.5mm²	N/A	2.16mm²	N/A
Avg. Power	1mW *$	N.R.	339uW	N.R.

* Angular orientation is also reported (3D+2/3D)
** For fluorescence-based method
*# Depends on penetration depth of the wired sensor
Can be enhanced by using bigger gradient coils
Only depth-FOV is relevant for RF
$ Reported for a single axis
$$ Reported for 2D US image area
#$ Center frequency
*$ Includes external sensor power
N.R.: Not Reported
N/A: Not Applicable

location, without performing any averaging. With positioning the approximate hole-location close to the center-region of the FOV, operation of the sensor in low-noise mode can be avoided.

The system is further evaluated in the presence of a Ti rod, as shown in Fig. 14 (a). Due to the extremely low magnetic susceptibility of Ti, there is practically no distortion (<0.1%) of the magnetic field in its presence, as evident from Fig. 14 (b). However, due to the presence of Ti metal right beneath the device, the WPT efficiency gets degraded due to the induced eddy currents in the metal. To improve the efficiency so as to keep the transmitted power well within the SAR standard of 1.6W/kg, a 6mm deep cavity is drilled from the surface of the rod and filled with PDMS (non-metallic, non-magnetic), inset in Fig. 14 (a). This achieves safe and robust power delivery up to an angular rotation of ±15° of the rod, which is the maximum deformation that can occur during flexion and torsion during orthopedic surgeries [7]. The depth of the cavity was optimized using simulations in HFSS, as shown in Fig. 14 (c).

The effect of interference from surgical tools and implants in the operation room (OR) is studied next. All tools can be classified as either magnetic (having high susceptibility of χ) or non-magnetic ($\chi \approx 0$), where the former cause distortion in the magnetic field gradient generated by the coils but the latter do not. Several localization experiments were conducted in the presence of both kinds of tools. For all non-magnetic tools, the error in the decoded position is independent of their presence, as shown in Fig. 14 (d) for one such type, and is thus <100µm. Most implants are non-magnetic and surgical tools made from non-magnetic materials are used routinely in the OR. For magnetic tools, the error is significant (2-8cm) only when the tools are in 1cm of proximity to the device. As the distance from the tools increases to 5cm, the error decreases to 1-5mm and falls below the 100µm threshold when the tools are ≥15cm away from the device. The results for one such tool are shown in Fig. 14 (e). Hence, the accuracy of our localization system is uncompromised in the presence of all non-magnetic surgical tools and implants and can be retained if all the magnetic tools are kept ≥15cm away from the device during the navigation and tracking phase.

Regarding medical safety in the OR, it is important to study the effect of magnetic force and magnetic torque on magnetic surgical tools when used in close proximity to our system. During the interference studies described above, no mechanical movement was observed in any of the magnetic surgical tools, even when placed right next to the device. This was the case both during the 100ms rise-time and the 10ms stable-time of the gradients, none of which led to any mechanical motion in the magnetic tools or the electrical equipment used. To verify this observation theoretically using the formulation described in [25], it is calculated that for Stainless Steel (used commonly for making surgical tools) with saturation magnetization M_s of 1.65T, the ratio of magnetic force to gravitational force and the ratio of magnetic torque to gravitational torque, are both less than 1 when the tools are kept ≥10cm away from the gradient coils. Magnetic forces and torques that are less than those produced by gravity are not expected to pose added risk to the patient [26]. It is expected that magnetic tools would be kept at least 15cm away from the coils and the devices, to retain the system's accuracy. At such distances, all magnetic tools and equipment can be safely used concurrently with our system.

For medical safety considerations, it is also important to study the effect of Peripheral Nerve Stimulation (PNS) due to gradient-switching performed by the coils. The 100ms rise-time for the gradients used in this work is significantly slower than the 0.1-1ms rise-time used in fast MRI scanners. PNS threshold is most commonly defined as the peak $d|B|/dt$, reported to be 43-57T/s in [27], which is sufficiently higher than our peak value of 0.4T/s (B≤40mT and 100ms rise-time). It is also worth noting that PNS effects are of concern when switching times are

in 0.1ms to ≈1ms range and are negligible when switching time is >5ms, given $|B|$<100mT [28]. Considering the rise-time along with the peak $d|B|/dt$ value, the International Electrotechnical Commission (IEC) thresholds for PNS and Cardiac Stimulations have a common asymptotic value of 20T/s at long rise-times (>5ms), thus implying complete safety of the gradient-switching employed in this work [29].

The system in this work is also capable of measuring the angular orientation of the device, which can be found after decoding the 3D location using field magnitudes. As the sensor transmits all the three orthogonal components (with sign information) of the magnetic field vector at its location, described by Eq. (4), the individual components can be compared one-to-one with those stored in the LUT to find the angular difference from the orientation used during characterization. This will provide complete position and orientation information of the devices relative to each other, which are critical for some surgical procedures. Authors in [30] have reported angular as well as position measurements for their magnetic tracking system, where localization of a magnet-robot is performed using an external array of 64 Hall-effect sensors. EndoScout developed by Robin Medical [31] uses a wired sensor (1cm^3 volume) that has an induced EMF in response to a known external magnetic field gradient. The gradient is produced by an MRI scanner since the system was developed primarily to localize sensors during MRI. However, the resolution of the system is limited to a few mm [32], mainly because of the large sensor volume and lack of integrated data processing. Also, the sensor is not wireless and is maneuvered using a catheter inside the body. Similarly, commercial systems using AC/DC EM-based tracking of sensors have been reported in the past [8] by NDI *Aurora*, Calypso, Polhemus and Ascension, but the requirements of high localization resolution, high FOV, high penetration depth, an integrated sensor with data-processing, wireless operation of the sensor, small size of the sensor, high sampling rate for real-time feedback, planarity and efficiency of the field-generator, safety and compatibility with metals – these are some of the crucial aspects that have not yet been met by any one single system. As a result, very few such systems have been clinically approved to be used as or along with implants during surgical navigation.

Table II shows the performance summary and comparison of our system with state-of-the-art localization techniques. The first part of the table compares our system-level specifications with other techniques used for localizing sensors and devices deep inside the body, based on X-Ray, Fluorescence, Optical, Ultrasound, RF, Laser, magnetic tracking, EM, and MRI-inspired. The second part compares our device-level specifications with other implantable/ingestible sensors and devices, most of which are AC/DC EM or RF-based, used for navigation and tracking *in vivo*. To the best of our knowledge, the resolution obtained by this system has the highest value to be reported. The FOV and penetration depth are also unprecedentedly high. The complete wireless operation of a device of this scale has not been shown before for localization applications. The sampling frequency of 7 Hz is currently limited by the ramp-up time of DC currents in the gradient coils. Future work would be to increase the sampling frequency and thus reduce the latency, perform angular orientation measurements in addition to the position (6D), and reduce the overall power and footprint of the implantable device by using a CMOS integrated 3D magnetic sensor.

VI. Conclusion

This paper presented a wireless 3D surgical navigation and tracking system that achieves <100μm localization error in 3D and in real time, using safe magnetic field gradients. The completely wireless operation of the implantable device and the significantly enhanced and scalable FOV, make the system highly suited for navigation during various high-precision surgeries and diagnostic procedures, thus eliminating the need for potentially harmful X-Ray fluoroscopy.

Acknowledgment

The authors acknowledge the contributions of M. Wang, S. Shah, W. Kuo, H. Sheng, A. Patil, K.-C. Chen and N. Phoole from MICS Lab; H. Davis from Shapiro Lab; A. Khachaturian from CHIC Lab; Dr. P.W. Goodwill, Dr. A.G. Siraki, Dr. J. Dorris, Dr. J. Kelly and Dr. S. Nikzad for insightful discussions; Muse Semiconductor for Chip fabrication; the editors and the anonymous reviewers for their highly valuable comments and feedback.

References

[1] W. M. Ricci et al., "Intramedullary Nailing of Femoral Shaft Fractures: Current Concepts," *JAAOS*, vol. 17, no. 5, pp. 296-305, 2009.

[2] A. Wang et al., "Wireless Capsule Endoscopy," *Gastrointestinal Endoscopy*, vol. 78, no. 6, pp. 805-815, 2013.

[3] U. Mezger et al., "Navigation in surgery," *Langenbeck's Archives of Surgery*, vol. 398, no. 4, pp. 501-514, 2013.

[4] H. Chen et al., "Advances in functional X-ray imaging techniques and contrast agents," *Physical chemistry chemical physics : PCCP*, vol. 14, no. 39, pp. 13469-86, 2012.

[5] H. M. Kremers et al., "Prevalence of Total Hip and Knee Replacement in the United States," *The Journal of bone and joint surgery. American volume*, vol. 97, no. 17, pp. 1386-97, 2015.

[6] B.A. Schueler, "The AAPM/RSNA Physics Tutorial for Residents General Overview of Fluoroscopic Imaging," *RadioGraphics*, vol. 20, no. 4, pp. 1115-26, 2000.

[7] T. Leloup et al., "A Novel Technique for Distal Locking of Intramedullary Nail Based on Two Non-constrained Fluoroscopic Images and Navigation," *IEEE Trans. Med. Imaging*, vol. 27, no. 9, pp. 1202-12, 2008

[8] A. M. Franz et al., "Electromagnetic Tracking in Medicine—A Review of Technology, Validation, and Applications," *IEEE Trans. Med. Imaging*, vol. 33, no. 8, pp. 1702-25, Aug. 2014.

[9] D. Vasisht et al., "In-body backscatter communication and localization," *Proceedings of the 2018 Conference of the ACM Special Interest Group on Data Communication* (*SIGCOMM '18*). Association for Computing Machinery, New York, NY, USA, pp. 132–146.

[10] F. Chen et al., "3D Catheter Shape Determination for Endovascular Navigation Using a Two-Step Particle Filter and Ultrasound Scanning," *IEEE Trans. Med. Imaging*, vol. 36, no. 3, pp. 685-695, 2017.

[11] F. Parent et al., "Intra-Arterial Image Guidance With Optical Frequency Domain Reflectometry Shape Sensing," *IEEE Trans. Med. Imaging*, vol. 38, no. 2, pp. 482-492, 2019.

[12] M. N. Oosterom, "Extending the Hybrid Surgical Guidance Concept With Freehand Fluorescence Tomography," *IEEE Trans. Med. Imaging*, vol. 39, no. 1, pp. 226-235, 2020.

[13] A. L. Simpson et al., "Comparison Study of Intraoperative Surface Acquisition Methods for Surgical Navigation," *IEEE Transactions on Biomedical Engineering*, vol. 60, no. 4, pp 1090-99, 2013.
[14] D. Formica et al., "Biological effects of exposure to magnetic resonance imaging: an overview," *BioMedical Eng. OnLine, vol.* 3, no. 11, 2004.
[15] V. Grover et al., "Magnetic Resonance Imaging: Principles and Techniques: Lessons for Clinicians," *Journal of Clinical and Experimental Hepatology,* vol. 5, no. 3, pp 246-55, 2015.
[16] M. Monge et al., "Localization of microscale devices in vivo using addressable transmitters operated as magnetic spins," *Nature Biomedical Engineering*, pp. 736-744, 2017.
[17] S. Sharma et al., December 2019, "Surgical alignment by magnetic field gradient localization," US Patent 20,190,388,105. http://www.freepatentsonline.com/y2019/0388105.html
[18] S. Sharma et al., "20.4 3D Surgical Alignment with 100μm Resolution Using Magnetic-Field Gradient-Based Localization," *2020 IEEE International Solid- State Circuits Conference - (ISSCC)*, San Francisco, CA, USA, 2020, pp. 318-320.
[19] R. Turner, "Gradient coil design: A review of methods," *Magnetic Resonance Imaging*, vol. 11, no. 7, pp 903-920, 1993.
[20] S.S. Hidalgo-Tobon, "Theory of gradient coil design methods for magnetic resonance imaging," *Concepts in Magnetic Resonance*, vol. 36A, no. 4, pp 223-242, 2010.
[21] J. Marques et al., "Low-Field MRI: An MR Physics Perspective," *Journal of Magnetic Resonance Imaging,* vol. 49, no. 6, pp. 1528-42, 2019.
[22] N5700 Series System DC Power Supplies by Keysight, Datasheet.
[23] N8700 Series System DC Power Supplies by Keysight, Datasheet.
[24] S.H. Kim et al., "Flexible, stretchable and implantable PDMS encapsulated cable for implantable medical device," *Biomedical Engineering Letters*, vol. 1, no. 199, 2011.
[25] J.A. Nyenhuis et al., "MRI and implanted medical devices: basic interactions with an emphasis on heating," *IEEE Transactions on Device and Materials Reliability*, vol. 5, no. 3, pp. 467-480, 2005.
[26] *Standard Test Method for Measurement of Magnetically Induced Torque on Medical Devices in the Magnetic Resonance Environment*, Standard F2213-17, ASTM International, 2017.
[27] C.L.G. Ham et al., "Peripheral nerve stimulation during MRI: Effects of high gradient amplitudes and switching rates," *Journal of Magnetic Resonance Imaging*, vol. 7, no. 5, pp. 933-937, 1997.
[28] D.J. Schaefer et al., "Review of patient safety in time-varying gradient fields," Journal of Magnetic Resonance Imaging, vol. 20, no. 1, pp. 20-29, 2000.
[29] V. Klein et al., "Investigating cardiac stimulation limits of MRI gradient coils using electromagnetic and electrophysiological simulations in human and canine body models," *Magnetic Resonance in Medicine*, vol. 85, no.2 pp. 1047-61, 2021.
[30] D. Son et al., "A 5-D Localization Method for a Magnetically Manipulated Untethered Robot using a 2-D Array of Hall-effect Sensors," *IEEE/ASME Transactions on Mechatronics*, vol. 21, no. 2, pp. 708-716, 2016.
[31] E. Nevo, February 2003, "Method and apparatus to estimate location and orientation of objects during magnetic resonance imaging," US Patent 6,516,213 B1. https://patents.google.com/patent/US6516213B1/en
[32] L. Pan et al., "Integration and evaluation of a gradient-based needle navigation system for percutaneous MR-guided interventions," *PloS one,* vol. 15, no. 7, July 2020.